Bioactive Materials 41 (2024) 627–639

Contents lists available at ScienceDirect

Bioactive Materials

journal homepage: www.keaipublishing.com/en/journals/bioactive-materials

Bioresponsive and transformable coacervate actuated by intestinal peristalsis for targeted treatment of intestinal bleeding and inflammation

Yuqi Peng [a,b], Xiaofen Luo [a,b], Xinyu Wang [c], Enling Hu [a,b], Ruiqi Xie [a,b], Fei Lu [a,b], Weiwei Ding [c], Fangyin Dai [a,b], Guangqian Lan [a,b], Bitao Lu [a,b,d,*]

[a] State Key Laboratory of Silkworm Genome Biology, College of Sericulture, Textile and Biomass Sciences, Southwest University, Chongqing, 400715, China
[b] Chongqing Engineering Research Center of Biomaterial Fiber and Modern Textile, Chongqing, 400715, China
[c] Division of Trauma and Surgical Intensive Care Unit, Research Institute of General Surgery, Jinling Hospital, Medical School of Nanjing University, Nanjing, 210002, Jiangsu Province, China
[d] School of Engineering, University of Birmingham, Edgbaston, Birmingham, UK

ARTICLE INFO

Keywords:
Intestinal ulcer bleeding
Bioadhesive coacervate
Intestinal peristalsis drive
Bioresponsive transformation
Adhesive hydrogel

ABSTRACT

Developing an oral in situ-forming hydrogel that targets the inflamed intestine to suppress bleeding ulcers and alleviate intestinal inflammation is crucial for effectively treating ulcerative colitis (UC). Here, inspired by sandcastle worm adhesives, we proposed a water-immiscible coacervate (EMNs-gel) with a programmed coacervate-to-hydrogel transition at inflammatory sites composed of dopa-rich silk fibroin matrix containing embedded inflammation-responsive core-shell nanoparticles. Driven by intestinal peristalsis, the EMNs-gel can be actuated forward and immediately transform into a hydrogel once contacting with the inflamed intestine to yield strong tissue adhesion, resulting from matrix metalloproteinases (MMPs)-triggered release of Fe^{3+} from embedded nanoparticles and rearrangement of polymer network of EMNs-gel on inflamed intestine surfaces. Extensive in vitro experiments and in vivo UC models confirmed the preferential hydrogelation behavior of EMNs-gel to inflamed intestine surfaces, achieving highly effective hemostasis, and displaying an extended residence time (> 48 h). This innovative EMNs-gel provides a non-invasive solution that accurately suppresses severe bleeding and improves intestinal homeostasis in UC, showcasing great potential for clinical applications.

1. Introduction

Disruption of the intestinal epithelial barrier and bleeding, key clinical manifestations of severe ulcerative colitis (UC), greatly diminish patients' quality of life and result in considerable economic costs [1,2]. To achieve effective hemostasis and prompt re-establishment of the mucosal epithelium, emergency barriers are required to inhibit microbial invasion, prevent blood loss, and decrease the risk of developing colorectal cancer [3,4]. Currently, oral delivery systems using enteric-coated tablets and capsules are favored for UC treatment due to their non-invasiveness, localized release, and elevated patient compliance [5,6]. Although various forms of oral drug delivery systems have been developed, insufficient residence time and low targeting efficiency for inflamed guts limit their clinical applications [7,8]. This challenge is primarily attributed to the harsh environment of the gut, which includes a large surface area, high motility, and humidity [9]. Hence, developing strategies to overcome the oral administration dilemma achieving targeting hemostasis and timely repair at inflammatory sites of the intestine remains a significant clinical challenge.

Inflammation-responsive therapy strategies, being actively developed as a potential alternative method for precise oral administration, aim to deliver drugs directly to lesion sites more effectively and safely [10,11]. The heightened expression and secretion of degradative enzymes, including esterase and matrix metalloproteinases (MMPs), are key characteristics of the mucosal surface in UC, particularly in regions of erosions and ulcerations [12,13]. Accordingly, the microparticle-based oral delivery system with enzyme-labile properties was designed to selectively bind to the inflamed mucosa and exert its therapeutic effect in response to the enzyme activities at inflammatory sites of the intestine [14]. As expected, these particles efficiently

Peer review under responsibility of KeAi Communications Co., Ltd.
* Corresponding author. State Key Laboratory of Silkworm Genome Biology, College of Sericulture, Textile and Biomass Sciences, Southwest University, Chongqing 400715, China.
E-mail addresses: b.lu@bham.ac.uk, lubitao000@email.edu.cn (B. Lu).

https://doi.org/10.1016/j.bioactmat.2024.08.020
Received 12 May 2024; Received in revised form 22 July 2024; Accepted 20 August 2024

released the drug at high concentrations of degradative enzymes, significantly reducing the dextran sulfate sodium (DSS)-induced inflammatory response in UC mice [15]. However, due to the complex microenvironment of the intestinal tract, these particles may be limited in their residence time and drug release effect by the adhesion and clearance mechanisms of the intestinal mucus layer. Therefore, these concerns provide an opportunity to design a novel strategy that combines active adhesion and prolonged residence time to expedite the hemostasis and healing of intestinal ulcers.

Intestinal motility, characterized by the intrinsic and continuous contraction during normal digestion, can be selected as a potentially active delivery system. Taking advantage of intestinal peristalsis, recent studies have demonstrated that precisely designed liquid coacervates can be propelled inside the intestine and efficiently cover the large intestinal surface area [16,17]. Due to their fluidity, water insolubility, and low surface tension, the coacervates can efficiently come into close contact with the tissue, providing a broader therapeutic effect [18]. Nevertheless, the extensive applicability of such materials has been limited, given that most liquid coacervates require increased frequency or dosage of administration to cover all lesions [19,20]. This limitation can be attributed to the absence of selective adhesion capability of these coacervates, resulting in adhesion to the initial contact area and failure to target the UC area accurately. To address this limitation, we propose a novel strategy that integrates peristaltic propulsion and inflammation-responsive mechanisms into a single material to achieve selective adhesion. Such material can be propelled by intestinal peristalsis and will exert robust adhesion once in contact with inflammatory sites. However, designing a coacervate material that combines both features remains a crucial challenge that urgently needs to be addressed.

In nature, sandcastle worms exhibit a fascinating ability to synthesize adhesive that enables them to aggregate sand particles and shell fragments for constructing their habitats under seawater [21]. This

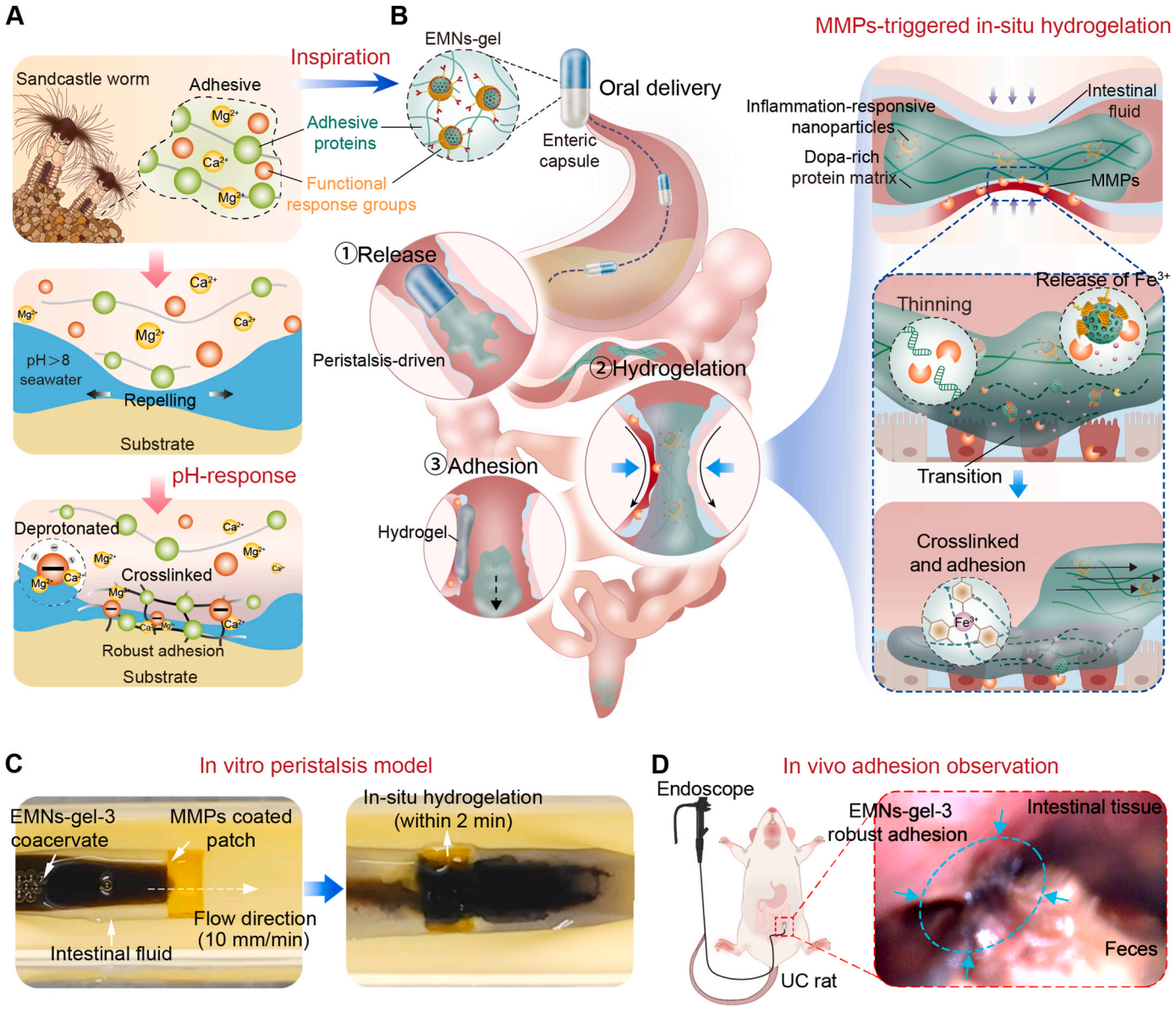

Fig. 1. Design and synthesis of sandcastle worm-inspired coacervate. A) Composition and adhesion mechanism of sandcastle worm adhesive. The dopa-rich protein matrix and functional response groups in the sandcastle worm adhesive cause robust adhesion by repelling water and pH-triggered cross-linking. B) Design of sandcastle worm-inspired coacervate and schematic illustration of EMNs-gel propelled by intestinal peristalsis and in-situ hydrogelation in response to MMPs at inflammatory sites. C) Photographs of sandcastle worm-inspired coacervate in vitro model achieving selective hydrogelation on MMPs coated patch under dynamic condition (with locomoted speed of 10 mm/min). D) Targeted hydrogelation of sandcastle worm-inspired coacervate at injury sites in the UC model.

adhesive achieves robust underwater adhesion by transitioning from a gel state to a solid state due to the dopa-rich protein matrix and functional response groups, primarily through a two-step process [22–24]. i) The dopa-rich protein matrix generated by the sandcastle worm, which consists of two types of anionic proteins and four types of cationic proteins, can displace or repel the water molecules from the substrate surface; ii) it can subsequently solidify on the surface of the substrate due to pH-triggered rapid crosslinking between polyphosphorylated

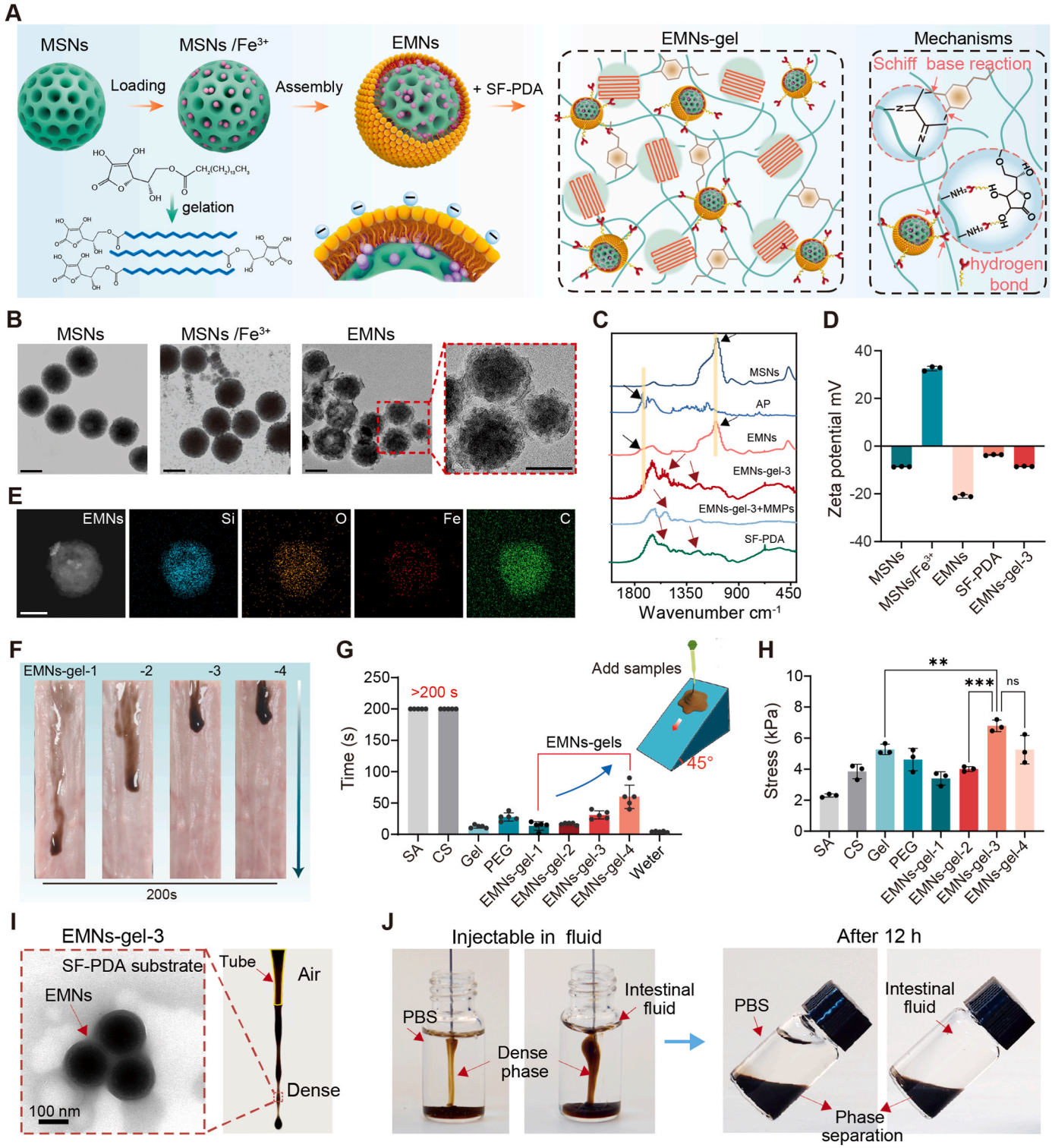

Fig. 2. Design and characterization of EMNs-gels. A) Schematic diagram of the preparation of EMNs-gels. B) TEM images of MSNs, MSNs/Fe^{3+}, and EMNs (scale bar is 100 μm). C) FTIR spectra of various samples. D) Zeta potential of various samples, n = 3. E) TEM mapping images of EMNs (scale bar is 100 μm). F) Images of coacervates with varying mixing ratios applied on a slope covered with intestines to visualize flow properties. G) The time required for candidate materials to flow from top to bottom of the intestine-covered slope, n = 5. Candidate materials include sodium alginate (SA), chitosan (CS), gelatin (Gel), polyethylene glycol-20000 (PEG), water, and EMNs-gel-1, 2, 3, and 4. H) The maximum shear strength of various coacervates tested based on the standard lap-shear setup, n = 3. I) TEM image of EMNs-gel-3 and image of EMNs-gel-3 extruded from the tube. J) Images of EMNs-gel-3 injected into artificial colonic fluid and PBS, and images of resting for 12 h.

protein and Ca^{2+} and Mg^{2+} (Fig. 1A). The programmed adhesion mechanism of the sandcastle worm inspired us to design a water-immiscible, transformable, and dopa-rich coacervate that can achieve selective adhesion underwater during intestinal peristalsis. We hypothesized that such a sandcastle worm-inspired coacervate could exert an in-situ hydrogel transformation once in contact with the UC area under the synergistic effects of intestinal peristalsis and inflammatory environments, thus providing a protective barrier for sustained hemostasis and UC repair.

In this research, an inflammation-responsive transformable coacervate (EMNs-gel), inspired by sandcastle worms, was proposed to achieve effectively targeted adhesion on the injury sites of the intestine to hinder bleeding and promote healing. Specifically, this novel coacervate consists of a dopa-rich silk fibroin protein matrix and inflammation-responsive nanoparticles containing mesoporous SiO_2 loaded with Fe^{3+} as the core and ascorbyl palmitate (AP) as the shell. The coacervate takes the form of a dense fluid through hydrogen bonding between the dopa-rich silk fibroin protein matrix and inflammation-responsive nanoparticles, which keeps them stable and water-immiscible in normal intestinal fluid and can be actuated forward by intestinal peristalsis. Upon being exposed to the inflammatory environments, the water-immiscible coacervate can displace the water molecules from the injury intestinal surface under peristaltic contraction to enable the inflammation-responsive nanoparticles to react with MMPs in the UC area, causing further crosslinking between dopa-rich silk fibroin protein and the injury tissue surface to form robust adhesion (Fig. 1B–D). Because of the synergistic effects of the peristaltic propulsion and inflammatory environment, this sandcastle worm-inspired coacervate is expected to attain highly efficient targeted adhesion, displaying significant promise for clinical applications in treating severe bleeding and injury induced by UC.

2. Results and discussion

2.1. Design and characterization of EMNs-gels

Specific pathological microenvironments in severe UC, such as increased secretion of endogenous enzymes in bleeding and inflammatory sites, were selected as triggering conditions to design the sandcastle worm-inspired coacervate capable of in-situ transformation of adhesive hydrogel layers. To implement the programmatically transformable mucoadhesive materials, endogenous enzyme-responsive mesoporous nanoparticles (EMNs) were first synthesized with a core comprising mesoporous silica nanoparticles loaded with Fe^{3+} (MSNs/Fe^{3+}) and an MMPs-degradable AP shell [25]. The resultant EMNs were then thoroughly mixed with silk fibroin grafted with polydopamine (SF-PDA) to form sandcastle worm-inspired coacervate with optimal flowability and on-demand adhesion properties (Fig. 2A). Driven by the intestine peristalsis, the EMNs-gel would spontaneously spread and the AP outer shell of EMNs could be hydrolyzed to liberate Fe^{3+} upon inflammatory conditions, which could quickly accelerate the hydrogelation of EMNs-gel triggering the in-situ formation of protective hydrogel barriers on the injured intestine tract.

Notably, EMNs were synthesized by thin-film rehydration through the assembly of the amphiphilic surface negatively charged AP on the surface of mesoporous silica nanoparticles (MSNs, ~130 nm) pre-loaded with Fe^{3+} [26]. The transmittance electron microscopy (TEM) images and particle size analysis revealed that EMNs (~180 nm) possessed an obvious core-shell structure comprising a mesoporous silica core with a thin outer layer with a thickness of ~50 nm (Fig. 2B and Fig. S5). Meanwhile, the FTIR curves of EMNs exhibited the absorption peaks of Si–O–Si (1071 cm^{-1}) [27], Si–H (796 cm^{-1} and at 988 cm^{-1}) [28], and C═O stretching of AP ester group (~1734 cm^{-1}) [29] (Fig. 2C). Furthermore, the deposition of AP on the surface showed the opposite charges compared to MSNs/Fe^{3+} nanoparticles (Fig. 2D). The above results revealed the successful assembly of AP on the surface of MSNs. Besides, TEM mapping images illustrated that the Fe element was uniformly encapsulated in EMNs (Fig. 2E). The loading content in EMNs was 2.67 g/mmol (Fig. S6). Next, the rheological property of EMNs-gel can be controlled by adjusting the ratio between EMNs and the SF-PDA matrix. These variations are labeled as EMNs-gel-1, 2, 3, and 4, corresponding to mass-to-volume ratios of 1:300, 1:200, 1:100, and 1:50, respectively. With the increase of mass fraction (MF) of the EMNs, the EMNs-gel displayed a transition from easily flowing fluids (EMNs-gel-1, 2) to stable fluid coacervates (EMNs-gel-3, 4) (Fig. S7). This phenomenon was attributed to supramolecular interactions, including hydrogen bonding and π–π interactions between the hydrophilic compounds (ascorbic acid) of AP and the catechol, amino, and phenyl groups derived from SF-PDA [30,31], which provide a substantial driving force that enhances molecular cohesion and facilitates the rapid assembly of a dense, viscous phase, thereby inducing coacervates formation [17]. Subsequently, the flowability and adhesive ability of EMNs-gel were quantitatively evaluated by flowing experiments on a 45° inclined plane (length 75 mm) precoated with the intestine and lap shear tests, respectively (Fig. 2F–H). Appropriate flowability and adhesion of the coacervate are crucial for its in-situ transformation into hydrogels intended for treating intestinal wounds. Among all candidates, it was observed that EMNs-gel-3 exhibited suitable flowability along with optimal adhesion strength (6.79 ± 0.37 kPa). In comparison, EMNs-gel-1, 2 with high flowability but low adhesion may flow off the wound surface before gelation, and EMNs-gel-4 with high adhesion but low flowability may tend to remain in the upper part of the intestine. Besides, the EMNs-gel-3 could form dense filaments with good shape fidelity when being extruded via dropper. The TEM image of EMNs-gel-3 demonstrated that the nanoparticles with core-shell structure labeled by red arrows could be embedded uniformly in the catechol-functionalized flexible polymer matrix to form the stable dense phase (Fig. 2I). Meanwhile, theoretical analysis of the total interfacial surface energy indicated that the EMNs in the SF-PDA protein matrix could maintain stability without phase separation, in alignment with the above-mentioned experimental results (Supplementary Note 1). Interestingly, the EMNs-gel-3 could maintain dense filaments upon injected (22G needle) into PBS and simulated intestinal fluid and showed a stable state of fluid-fluid phase separation even after 12 h, indicating a subtle balance of interfacial interaction between the EMNs-gel-3 and fluid (Fig. 2J and Mov. S1). Taken together, the suitable flowability and water-immiscibility of EMNs-gel-3 allow it to spread spontaneously on the inner wall of the intestine upon intestine peristalsis. Thus, the EMNs-gel-3 with a relatively higher mass fraction of the nanoparticle was selected as the optimal candidate in this study.

2.2. Mechanism of MMPs-triggered transformation of EMNs-gels into hydrogels

To comprehend the performance and mechanism of EMNs-gel transformation in inflammatory settings, MMPs as typical endogenous enzymes overexpressed at bleeding and inflammatory sites, were utilized to construct a series of in vitro characterizations. Initially, the conversion of EMNs-gels to hydrogels at different mass-to-volume ratios of EMNs to SF-PDA was evaluated using time sweep rheology analysis, and the time taken for the transformation was counted. At ratios of 1:300 and 1:200, the storage modulus (G′) was lower than the loss modulus (G″) after the introduction of MMPs (200 U/mL) during the initial 450 s, suggesting no obvious hydrogel formation within 450 s. In contrast, the hydrogelation process could be observed within 300 s at a ratio of 1:100, as indicated by the crossover of G′ and G″ curves and digital photographs (Fig. 3B and C). Additionally, the hydrogel created using EMNs-gel-3 could easily adhere to a glass rod and transform into long and viscous fibers when stretched in a water environment (Fig. 3D). When the ratio increased to 1:50, the hydrogel transition occurred within seconds after incubation with MMPs. However, the resulting hydrogel displayed weak underwater adhesion ability due to over-

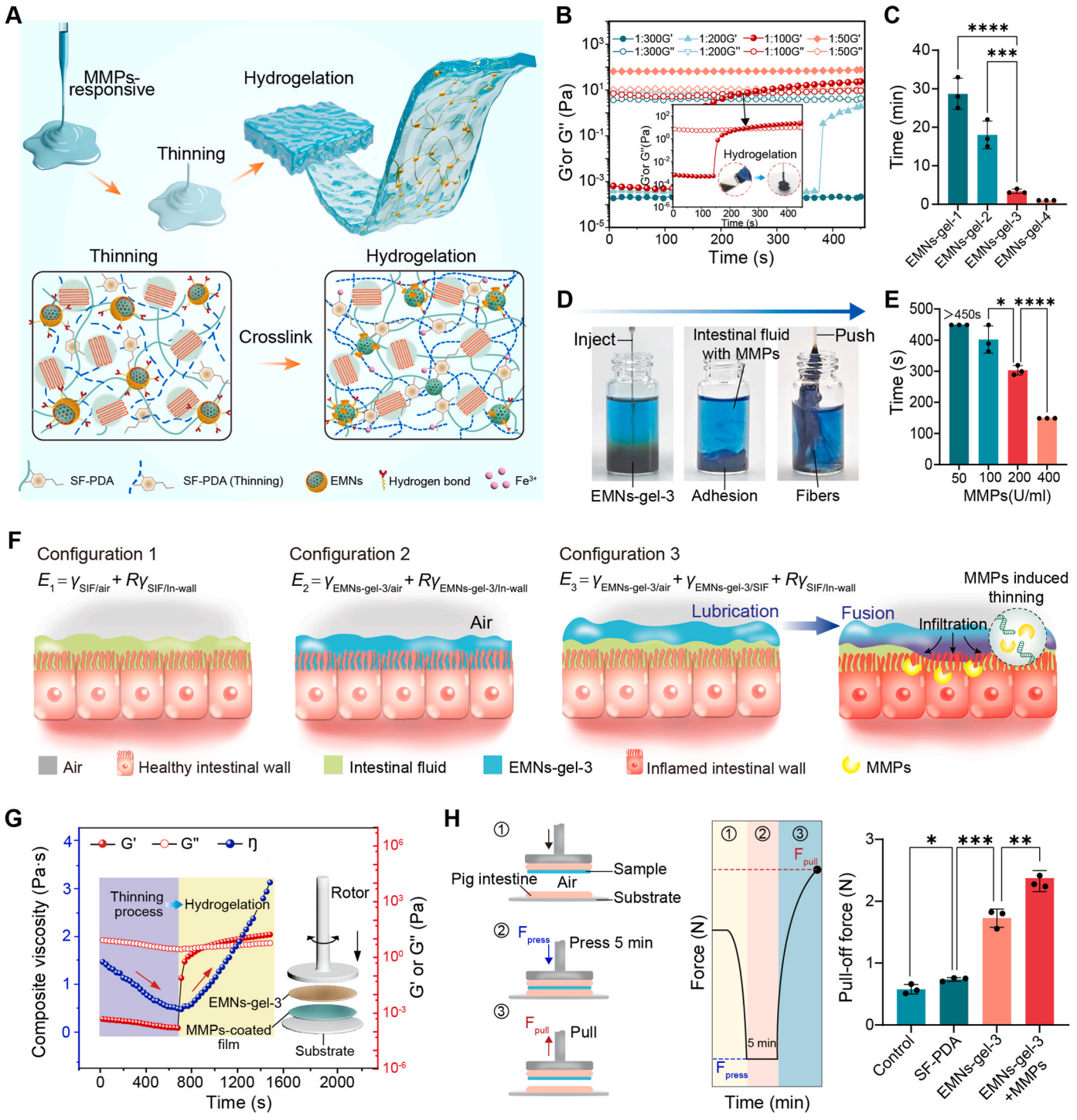

Fig. 3. Mechanism of MMPs-triggered transformation of EMNs-gels into hydrogels. A) The mechanism of hydrogelation of EMNs-gel-3 in response to MMPs. B) Rheological properties of EMNs-gel-1, 2, 3, and 4 with the addition of MMPs (200 U/mL) under time sweeps and C) corresponding gelation times. D) Images of EMNs-gel-3 in intestinal fluid reacting with MMPs (200 U/mL) to form the hydrogel. E) The gelation time of EMNs-gel-3 exposed to various concentrations of MMPs. F) Schematic illustrations of configurations for the surface energy of EMNs-gel-3 on normal and inflammatory tissue. G) Rheological experiments recording the viscosity, G′ and G″ changes of EMNs-gel-3 on MMPs-coated intestine (200 U/mL). H) Schematic diagram of pull-off test and statistics of maximum pull-off force. Each set of tests was independently repeated 3 times.

crosslinking by Fe^{3+} which reduced the number of surface adhesive groups [32,33] (Figs. S8A and B). Furthermore, by adjusting the MMPs concentration, the hydrogelation time of EMNs-gel-3 changed from 15 min to 5 min, and further to less than 150 s as the MMPs concentration was increased from 50 to 400 U/mL (Fig. 3E and Fig. S9A). To clearly illustrate the hydrogelation process, the Fe^{3+} release kinetics in EMNs were quantitatively tested. The addition of MMPs caused the hydrolysis of surface AP in EMNs, and simultaneously induced a rapid release of Fe^{3+}, resulting in a concentration of 35 mmol/L within 5 min (Figs. S9B and C). Furthermore, TEM and scanning electron microscopy (SEM) were utilized to record microstructure changes of EMNs-gel-3 before and after treatment with MMPs. Time-dependent TEM images displayed the hydrolysis of the out-layer of EMNs and the formation of network structures (Fig. S9D). SEM images revealed a denser pore structure in the

hydrogel, highlighting the rearrangement of the polymer structure triggered by MMPs (Fig. S9E). These findings confirmed that EMNs-gel-3 can be transformed into hydrogel upon MMPs activation.

To ensure the accurate transformation in bleeding and inflammation setting, the water-immiscible EMNs-gel-3 should satisfy two criteria: (1) After being infused into the intestine, this kind of coacervate can be propelled forward by peristalsis without mutual dissolution in a non-inflammatory intestinal setting; (2) can undergo an in-situ hydrogel transformation once contacting sites of bleeding and inflammation. To confirm the first requirement, the locomotion behavior of EMNs-gel-3 upon peristalsis was illustrated by comparing the various total surface energies of individual wetting configurations. Specifically, Configuration 3 represented the scenario where the intestine wall (In-wall) was completely wetted by intestinal fluid (SIF) with EMNs-gel-3 floating on the top. Configurations 1 and 2 represented the scenarios where the intestine wall was completely by intestinal fluid or EMNs-gel-3, respectively (Fig. 3F). To ensure the EMNs-gel-3 could be propelled steadily, Configurations 1 and 3 should always have a lower energy state than Configuration 2, meaning that $\Delta E_1 = E_2 - E_1 > 0$ and $\Delta E_2 = E_2 - E_3 > 0$. These equations can be calculated as (Supplementary Note 2)

$$\Delta E_1 = R\left(\gamma_{SIF}\cos\theta_{SIF/In-wall} - \gamma_{EMNs-gel-3}\cos\theta_{EMNs-gel-3/In-wall}\right) + \gamma_{EMNs-gel-3/air} - \gamma_{SIF/air} > 0 \quad (1)$$

$$\Delta E_2 = R\left(\gamma_{SIF}\cos\theta_{SIF/In-wall} - \gamma_{EMNs-gel-3}\cos\theta_{EMNs-gel-3/In-wall}\right) - \gamma_{EMNs-gel-3/SIF} > 0 \quad (2)$$

where E_1, E_2, and E_3 correspond to the total interfacial energies per unit area for Configurations 1, 2, and 3, respectively. The R, $\gamma_{x/y}$, and γ_x represent the roughness factor, the interfacial energy between x and y, and the surface tension of a fluid x, respectively. Besides, $\theta_{x/y}$ represents the contact angle of x on y. By substituting the values of parameters (R = 2, $\gamma_{EMNs\text{-}gel\text{-}3}$ = 44.1 mN m^{-1}, γ_{SIF} = 30.6 mN m^{-1}, $\gamma_{EMNs\text{-}gel\text{-}3/SIF}$ = 2.38 mN m^{-1}, $\theta_{SIF/In\text{-}wall}$ = 10°, $\theta_{EMNs\text{-}gel\text{-}3/In\text{-}wall}$ = 49.2°) into equations (1) and (2), the ΔE_1 and ΔE_2 was 15.9228 mN m^{-1} and 0.0428 mN m^{-1}, respectively. It is demonstrated that inequality in the equation denotes fulfillment, illustrating that the EMNs-gel-3 cannot be displaced or diluted by intestinal fluid during locomotion. Meanwhile, the intestinal fluid could form a lubricating layer between water-immiscible EMNs-gel-3 and tissue to reduce the internal friction according to previous studies [34], ensuring a high flowability of EMNs-gel-3 and avoiding premature loss on the forefront of the intestine.

For the second criterion, the rheological property of EMNs-gel-3 on the surface of the MMPs-coated intestine was further measured more practically. Interestingly, the rheological analysis indicated that EMNs-gel-3 displayed a thinning behavior with viscosity decreasing from 1.464 Pa s to 0.462 Pa s in the initial 10 min, which was mainly due to the MMPs triggering the hydrolysis of the ester bonds in the AP and the cleavage of the long chains of the silk fibroin protein molecules [25,35,36] (Fig. 3G and Fig. S10). This phenomenon suggested a decomposition of the interconnected network and a reduction in surface tension within EMNs-gel-3, leading to a transformation from a water-immiscible state to a water-soluble state. During the thinning process, the Fe^{3+} gradually released from EMNs particles triggered by MMPs and simultaneously diffused within EMNs-gel-3 to induce a rapid chemical crosslink between themselves and the tissue surface to reverse the thinning process, resulting in a dense hydrogel layer on the wet tissue surface (Fig. 3A). The chemical crosslink, including the chelation effect between Fe^{3+} and phenolic hydroxyl and quinone group in SF-PDA, along with the covalent crosslinks between quinone group and amine groups abundant in both intestinal surface and SF-PDA wound trap water molecules to provide a stable adhesive hydrogel [37]. To further demonstrate the MMPs-triggered rearrangement of interfacial interaction, the pull-off test model was established to test the in-situ adhesion mechanical ability of EMNs-gel-3 in a simulated intestinal fluid bath. After applying gentle pressure for 5 min ($\leq$ 10 kPa), the EMNs-gel-3 on the MMPs coated intestine showed a relatively high pull-off force, whereas the group without MMPs cannot form stable adhesion (Fig. 3H). Concurrently, as the contact time of EMNs-gel-3 on the MMPs-coated intestine increased, the pull-off force initially increased and then reached a plateau when the contact time exceeded 15 min (Fig. S11). These results demonstrated that MMPs could effectively trigger the hydrogelation of EMNs-gel-3 and the rearrangement of interfacial interactions in the presence of simulated intestinal fluid, which is consistent with the above rheological analysis. Notably, when in contact with wet intestinal surfaces containing MMPs, the temporary thinning process may allow the infiltration of EMNs-gel-3 to the bleeding and inflammatory sites and facilitate the rearrangement of interfacial interactions, which further provides an enormous potential to realize in situ hydrogelation and adhesion. This MMPs-triggered transition to adhesive hydrogels upon contact with bleeding and inflammatory intestine surfaces could potentially offer a protective hydrogel layer and avoid tissue damage caused by traditional surgical procedures.

2.3. Adhesion mechanical test, dynamic adhesion property in vitro and vivo model

To evaluate the coacervate stability and durability of the transformed hydrogels, EMNs-gel-3 was applied onto fresh ex-vivo intestines that had been pre-coated with MMPs solution at 37 °C for 30 min. The results showed that a dark-brown hydrogel layer can form in situ on the MMPs deposited section of the intestinal surface without pressure within 5 min, demonstrating a strong MMPs-dependent hydrogelation behavior due to the high reactivity between AP and MMPs (Fig. S12). Besides, the resulting hydrogel can firmly adhere to the intestinal surface, as indicated by its capacity to withstand extensive stretching and twisting both in air and underwater conditions (Fig. S13A). Subsequently, soaking the tissue with adhesive hydrogel in simulated intestinal fluid at 37 °C for 24 h, the hydrogel coatings remained firmly attached without detaching from the tissue surface, indicating the robust adhesion capability to withstand mechanical challenges and the durable adhesion performance to the wet intestinal surface (Fig. S13B). Meanwhile, the resulting hydrogel could also remain stable without degradation after being incubated in artificial colon fluid at 37 °C for 72 h, showing a good digestive enzyme-resistant ability (Fig. S13C). To quantitatively analyze the adhesion behavior of transformed hydrogel, we quantified the adhesion strength between the hydrogel and intestinal tissue through lap shear and 180° peel tests. The EMNs-gel-3 exhibited a strong adhesion performance on the MMPs-covered intestinal surface with a peeling strength of 61.78 ± 4.27 Nm^{-1} and shear strengths of 57.81 ± 9.08 kPa (Figs. S13D and E). Moreover, the EMNs-gel-3 was also applicable to blood and MMPs-covered intestinal surfaces, showing superior adhesion performance with peeling strength of more than 92.28 Nm^{-1} and shear strength of more than 87.83 kPa, owing to the high reactivity between natural nucleophiles (amido bond, thiol, and amines) in blood proteins and abundant quinone groups in EMNs-gel-3. The ability of the EMNs-gel-3 to generate better adhesion on blood and MMPs-coated intestinal surface could be advantageous for rapid coagulation in injury.

The harsh environment of the injured intestine including physiological peristalsis and wetted surface remains challenging for targeted adhesion. Therefore, the in-situ hydrogelation behavior of EMNs-gel-3 on the injury site of the intestine was further observed and investigated under more realistic conditions via an in vitro dynamic model. As shown in Fig. 4A, it was equipped with a motorized gear system to simulate the natural intestinal peristaltic action, along with a hydrogel patch containing MMPs to simulate the injury site. The integrated worm gear and drive wheel ensured the locomotion of EMNs-gel-3 on hydrogel patches. The treated hydrogel patches slowly released MMPs in simulated intestinal fluid (Fig. S14). As shown in Fig. 4B and Mov. S2, the

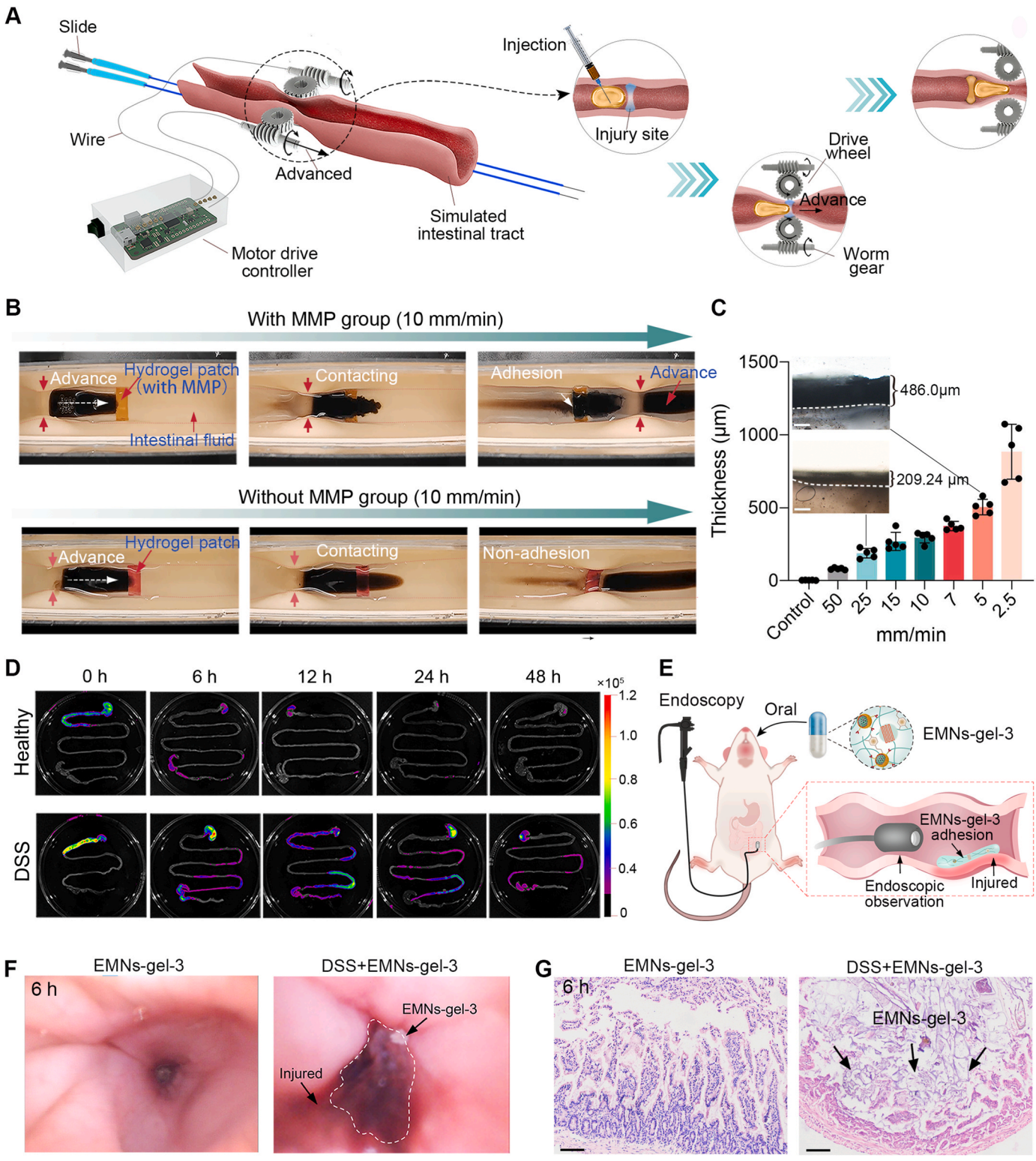

Fig. 4. Dynamic adhesion property in vitro and vivo model. A) Schematic diagram of the dynamic model of intestinal peristalsis in vitro. B) Photographs of EMNs-gel-3 in vitro model achieving selective hydrogelation under dynamic conditions (with locomoted speed of 10 mm/min). C) The corresponding thickness of the hydrogel layer on the MMPs-coated patch at different locomotion speeds (scale bar is 100 μm, n = 5). D) The fluorescence imaging of healthy mice and UC mice at different time points (0, 6, 12, 24, and 48 h) after oral administration of EMNs-gel-3. E) Schematic diagram of endoscopic observation after administration of EMNs-gel-3 in rats. F) Endoscopic images of rats 6 h after administration of EMNs-gel-3. G) H&E staining sections of mice 6 h after administration of EMNs-gel-3 (scale bar is 100 μm).

EMNs-gel-3 was steadily locomoted underwater at a speed of 10 mm/min without any dilution and could effectively adhere to the MMPs-coated hydrogel patch. This locomotion speed is higher than the speed of food peristalsis in the UC intestine (small bowel ~7 mm/min, colon ~1 mm/min) [38–41], indicating that the hydrogelation and adhesion of EMNs-gel-3 could overcome the resistance of peristalsis and underwater environment. By contrast, the EMNs-gel-3 cannot leave any trace after crossing the hydrogel patch without MMPs (Fig. 4B and Mov. S3). Furthermore, the thickness and microstructure of the in-situ formed hydrogel layers were kinetically analyzed using an optical microscope and SEM under various locomotion speeds (50, 25, 15, 7, 5, 2.5 mm/min). Surprisingly, the transformed hydrogel layer with thicknesses of more than 81.83 ± 6.97 μm displayed uniform network structure even when the locomotion speed of fluid increased to 50 mm/min, demonstrating the high sensitivity and stability of MMPs triggering EMNs-gel-3 to transform into adhesive hydrogels (Fig. 4C and Figs. S15A and B).

The in-situ transformation of EMNs-gel-3 was further evaluated using in vivo. The C57BL/6 mice (male, 8–12 weeks) with or without UC were fed with commercial enteric capsules loaded with Cy5.5-labeled EMNs-gel-3 to confirm the in-situ transformation and adhesion behavior through the in vivo fluorescence imaging method. As expected, in mice with intestinal injury group, the EMNs-gel-3 adhered to the intestinal tract for at least 48 h as proved by the strong fluorescence signal. while in the healthy group, the EMNs-gel-3 was metabolized completely within 12 h (Fig. 4D and Fig. S16). This behavior in agreement with the results in vitro dynamic mode test demonstrated that EMNs-gel-3 could

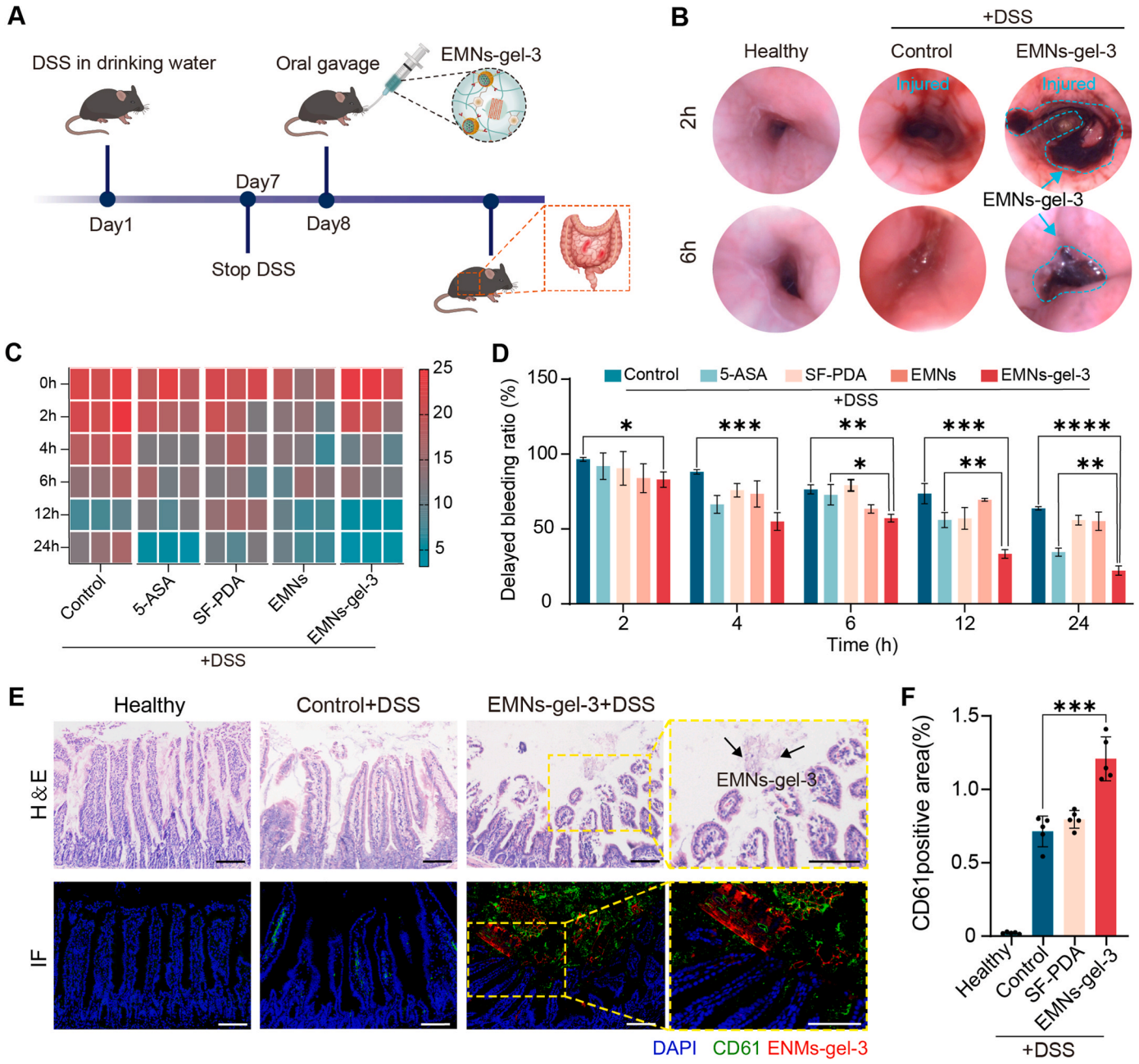

Fig. 5. Rapid hemostasis ability of EMNs-gel-3 in acute UC. A) Experimental design. Mice were given sterile water or water containing 3 % DSS for 7 days. The oral treatment was given from day 8. B) Endoscopic images of rats after oral administration of EMNs-gel-3 for 2 h and 6 h. C) Heat map of fecal occult blood content and D) rate of delayed hemorrhage in mice (n = 5). E) Representative H&E staining and immunofluorescence (CD61 green, EMNs-gel-3 red, and 4′,6-diamidino-2-phenylindole [DAPI] blue) images of UC mouse intestinal tissue (scale bar is 100 μm). F) Semi-quantitative analysis of CD61 fluorescence intensity in mouse intestinal tissue, n = 5.

form a protective barrier with prolonged retention capacity. After administering a commercial capsule containing EMNs-gel-3 to a rat model of UC, endoscopic observation revealed that EMNs-gel-3 selectively adhered to the inflamed sections of the intestinal wall, forming a hydrogel coating (Fig. 4E and F and Mov. S4-5). To further investigate the selective targeting capabilities of EMNs-gel-3, we analyzed the intestinal tissues of treated UC mice using hematoxylin and eosin (H&E) staining. The findings corroborated our initial observations, with EMNs-gel-3 exclusively present in the intestinal tissues of mice with induced injuries (Fig. 4G). Taken together, these findings from in vitro and in vivo experiments verify that the transformed hydrogel has robust and durable adhesion capabilities. This potentially provides an effective approach to prevent intestinal injury by forming protective hydrogel layers in the situs. As such, EMNs-gel-3 showed immense potential as a targeted treatment agent for intestinal inflammation and bleeding, offering a new approach to treating UC.

2.4. Rapid hemostasis ability of EMNs-gel-3 in acute UC

All animal experiments were performed following the protocols approved by the European Union Animal Experimentation Directive 2010/63/EU and by the protocols approved by the National Center for Experimental Teaching of Animal Science, Southwest University, China. The approval number is SWU_LAC_202110616. All mice and rats were purchased from Hunan Saijia Laboratory Animal Co. All animal experiments were approved by the Ethics Committee for Animal Experiments of Southwest University (Approval No. SYXK 2020-0006) and were conducted following the committee's guidelines for animal handling.

The results of in vitro coagulation and biocompatibility assays showed that EMNs-gel-3 had superior hemostatic ability and low biotoxicity (Supplementary Notes 3 and 4). To dynamically demonstrate the hemostatic properties of EMNs-gel-3 in vivo, the DSS-induced acute UC rat and mice models were created. Sprague Dawley (SD) rats (male, ~250 g) and C57BL/6 mice (male, ~25 g) were fed with sterile water containing 3 % DSS for 7 days to establish the UC models (Fig. 5A). After that, the EMNs-gel-3 loaded in commercial enteric capsules were administered through oral gavages and the hemostatic effect was confirmed by the endoscope and histological analysis. The endoscopic images revealed that the healthy rat showed a smooth and intact intestinal wall but was damaged with bleeding and inflammatory signs after treatment with DSS. As expected, the EMNs-gel-3 could effectively alleviate intestinal bleeding in the acute colitis model as evidenced by the formation of a distinct dark purple hydrogel layer on the intestinal wall after 2 h of administration, indicating the outstanding targeted transition and adhesion ability of EMNs-gel-3. At 6 h after application, the transformed hydrogel layer can still adhere to the injury sites without apparent bleeding traces, showing good hemostatic sealing effects and a long-term residence (Fig. 5B and Mov. S5-9). In contrast, persistent bleeding was still observed after 24 h in the colitis models of the untreated and SF-PDA-treated groups (Fig. S17A). Moreover, the amount of delayed bleeding was tested to confirm the hemostatic effects of EMNs-gel-3 via qualitative fecal occult blood test kits. The results shown in Fig. 5C and Fig. S18 indicate that the lowest fecal blood content was observed in the EMNs-gel-3 group after 12 h of treatment, suggesting that EMNs-gel-3 is more efficient in the treatment of bleeding in acute UC when compared to the commercially available antiemetic,5-aminosalicylic acid (5-ASA), and the other control groups. Meanwhile, the statistics of delayed bleeding rate derived from fecal occult blood test kits also confirmed the above findings, indicating that the delayed bleeding rate was significantly reduced 24 h after the administration of EMNs-gel-3 (Fig. 5D). Hence, these results conclusively illustrated that EMNs-gel-3 possessed the capability to transform into a hydrogel layer at the inflammatory site of the intestine, achieving highly effective hemostasis.

Subsequently, the in vivo hemostatic mechanism of EMNs-gel-3 was investigated through histological analysis. The immunofluorescence analysis of markers (CD61 for platelets, Rhodamine B for transformed hydrogel) shows that the green fluorescent labeled platelets can be observed in the network pore structure of the transformed hydrogel (Fig. 5E and Fig. S17B). Notably, the immunofluorescence intensity analysis indicated that the EMNs-gel-3 induced more platelet adhesion and aggregation around the wounded intestine tissue, significantly superior to that in the control group (Fig. 5F). This is because the gelation properties of EMNs-gel-3 make it a physical barrier against blood loss, which will physically force platelets toward the damaged blood vessel. On the other hand, the catechol fraction of the hydrogel promotes aggregation and adhesion of erythrocytes and platelets [42]. Therefore, under intestinal peristalsis actuation, EMNs-gel-3 could effectively inhibit intestine bleeding through the in-situ formation of a robust physical hydrogel barrier and accelerating the aggregation of platelets.

2.5. Excellent healing effect of EMNs-gel-3 on acute UC

After demonstrating the targeted adhesion and strong hemostatic ability of EMNs-gel-3 in rats, we further evaluated the therapeutic efficacy with in-situ transformed hydrogel against acute UC. The experimental approach was schematically depicted in Fig. 6A. In comparison with the treatments of the 5-ASA group, the mice treated with EMNs-gel-3 exhibited increased body weight, extended colon length, decreased disease activity index (DAI), and reduced spleen weight, indicating a potential anti-inflammatory effect (Fig. 6B–D and Figs. S19–20). Notably, the mice treated with SF-PDA and EMNs had shorter colons and a higher spleen weight compared to those in the EMNs-gel-3 group, demonstrating an enhanced therapeutic effect of EMNs-gel-3 assembled from SF-PDA and EMNs. Furthermore, the H&E staining section revealed that the mice treated with EMNs-gel-3 could preserve the integrity of the intestine epithelium, reduce the intestinal villi damage, and inhibit the infiltration of pro-inflammatory cells in the mucosa, confirming a significantly better efficacy in alleviating colitis compared to 5-ASA. Moreover, a much higher expression of proliferating cell nuclear antigen (PCNA), a crucial tissue marker of cell proliferation (red arrows), was observed in the groups with the administration of EMNs-gel-3 (Fig. 6E and F). Notably, previous studies demonstrated that PDA and AP could efficiently eliminate reactive oxygen species (ROS) and regulate macrophage differentiation [43,44]. Therefore, the protein levels of nitric oxide synthase (iNOS, a marker for type 1 macrophages) and arginase-1 (a marker for type 2 macrophages) in intestine tissue were quantitatively evaluated using immunohistochemical fluorescence staining. The findings revealed that treatment with EMNs-gel-3 significantly improved the expression of arginase-1 while decreasing the expression of iNOS, suggesting that EMNs-gel-3 promotes the differentiation of M2 macrophages and inhibits M1 macrophages in DSS-induced colitis (Fig. 6G–I). Additionally, the treatment of EMNs-gel-3 significantly reduced the expression of pro-inflammatory cytokines including IL-6, IL-1β, and TNF-α, while enhancing the expression of the transforming growth factor-β (TGF-β) (Fig. 6J-M). These findings verified that the in-situ hydrogel layer could alleviate the DSS-induced colitis by decreasing the inflammatory response.

The intestinal flora dysbiosis may cause the exacerbation of the progression of UC. Normally, the intestinal flora is in balance with the host's immune system and assists in digestion, absorption, and metabolism. However, when the gut flora is dysbiotic, the number of harmful bacteria may increase while the number of beneficial bacteria may decrease, leading to an increased inflammatory response in the gut. Thus, restoration of the gut microbiota and immune homeostasis can complement each other in the successful treatment of UC [45]. To investigate the regulatory effects of EMNs-gel-3 on the intestinal microbiota, the composition of the intestinal flora was analyzed by sequencing the 16S ribosomal RNA (rRNA) gene amplicon in fecal samples. Analysis of 16S rRNA sequencing on day 8 showed that EMNs-gel-3 treatment indeed significantly increased bacterial abundance (observed operational taxonomic units, OTUs) and α-diversity

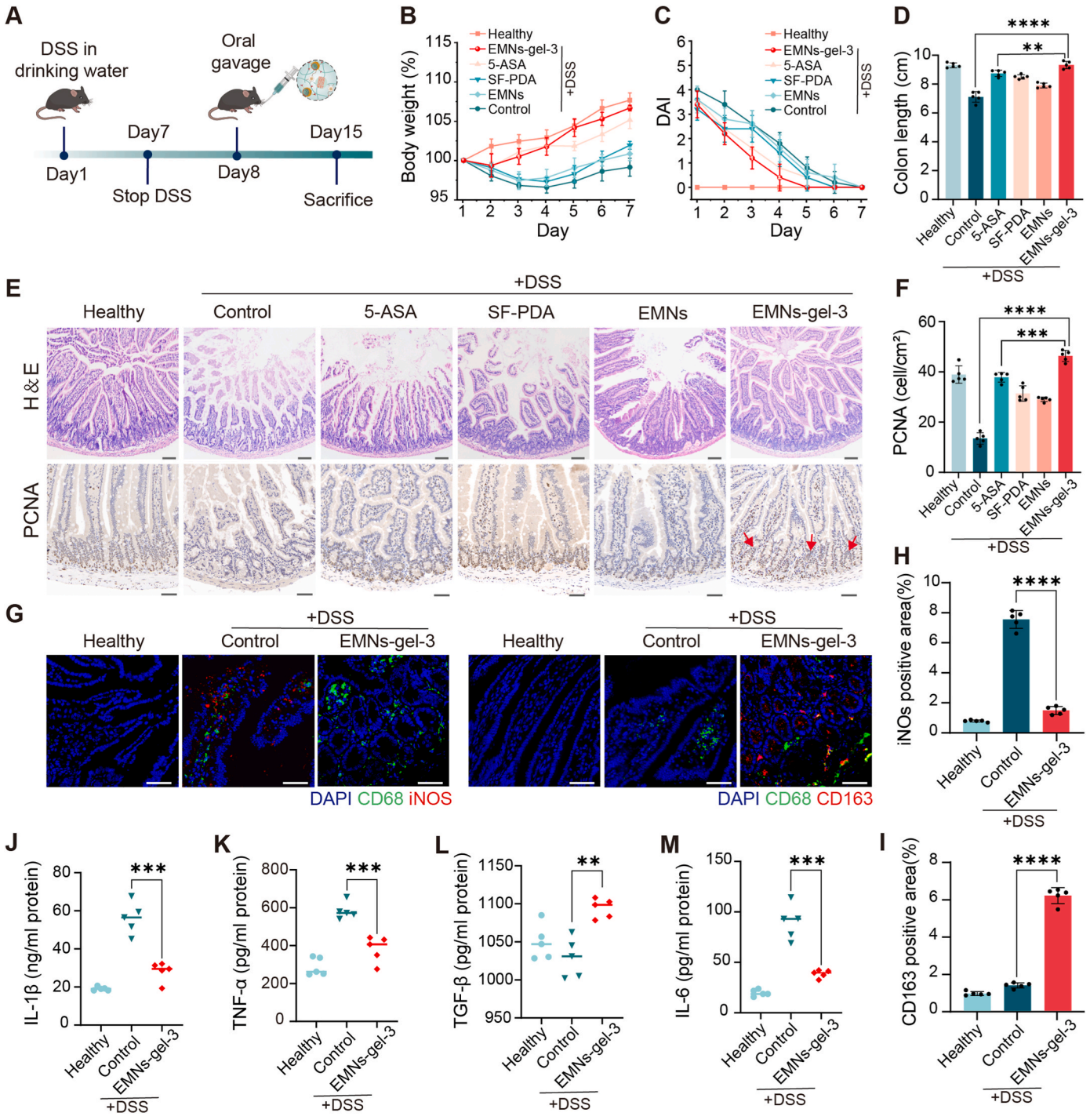

Fig. 6. EMNs-gel-3 showed enhanced therapeutic efficacy by inhibiting intestinal inflammation and facilitating tissue healing. A) Experimental design. Sterile water containing 3 % DSS. B) Changes in body weight and C) DAI scores of mice in each group for 7 consecutive days after stopping drinking DSS. D) Measure and analyze colon length. E) Images of representative H&E staining (scale bar is 100 μm) and PCNA staining (scale bar is 50 μm) of intestinal tissues from each group. F) Semi-quantitative analysis of PCNA. G) Immunofluorescence analysis of M1 (iNOS red, CD68 green, and DAPI blue) and M2 (CD163 red, CD68 green, and DAPI blue) in gut tissue visualized under confocal microscopy (scale bar is 25 μm). H) and I) Semi-quantitative analysis of fluorescence intensity of iNOS and CD163. J-M) The serum concentration of IL-1β, TNF-α, IL-6, and TGF-β. n = 5 biologically independent mice per group.

(Chao and Shannon indices) in UC mice (Fig. 7A–C). Principal coordinate analysis (PCoA) was used to evaluate the overall gut flora. There was a significant change in the clustering of gut bacterial composition in the control group compared to the healthy group, indicating the dysfunctional gut flora following DSS administration. As expected, the EMNs-gel-3 group cluster was close to that of the healthy group, suggesting that EMNs-gel-3 treatment alleviated the ecological dysregulation of colitis (Fig. 7D). The Venn diagram illustrated the data on common and unique taxa of the gut flora across the three groups (Fig. 7E). The general enterobacterial composition at the phylum (Fig. 7F) and family level (Fig. 7G) for each group was displayed in bar charts and heat maps, respectively. The gut flora composition was analyzed at the phylum level, showing the highest similarity in microbial composition between the healthy and EMNs-gel-3 groups based on

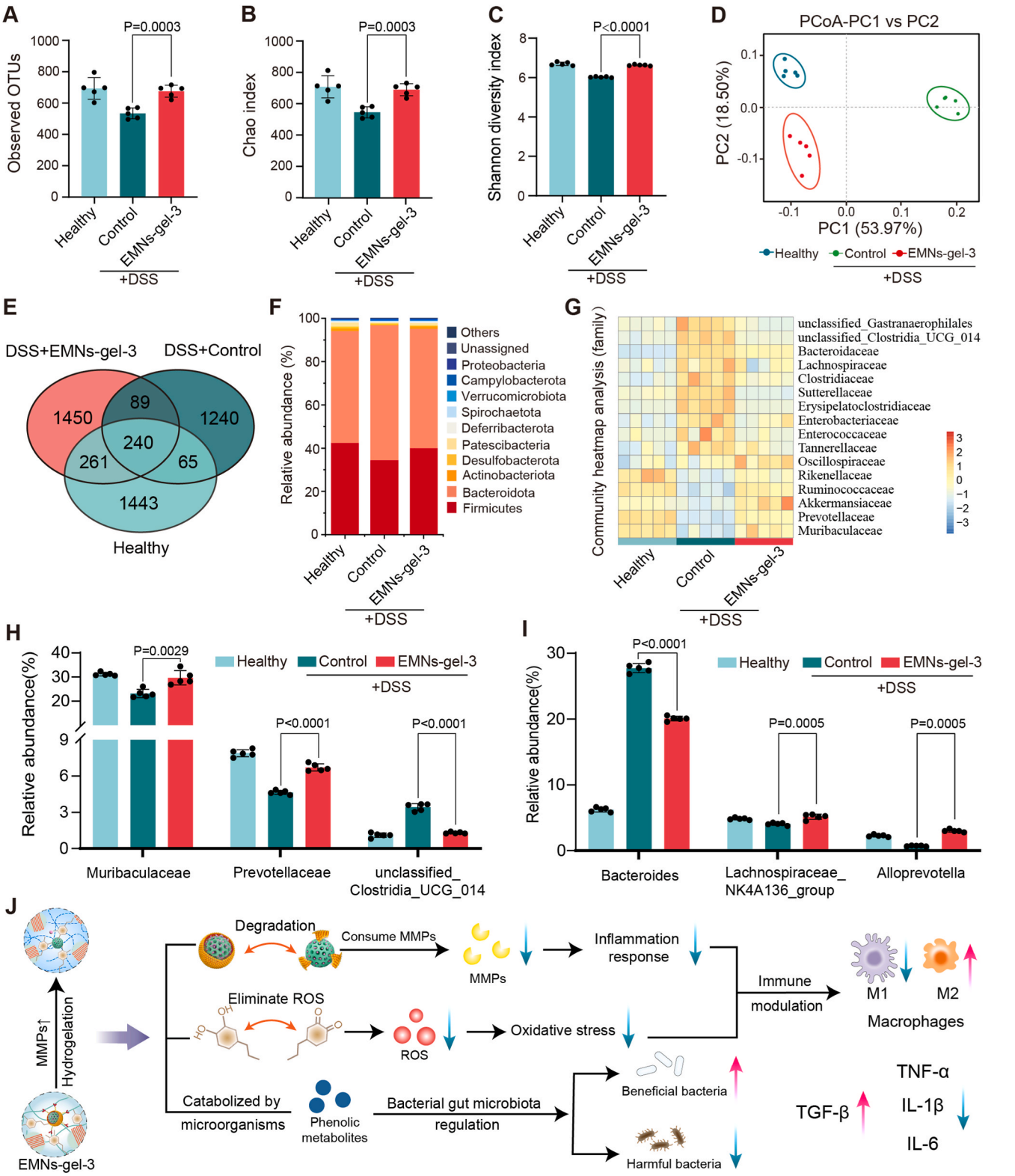

Fig. 7. Regulation of gut microbiota by EMNs-gel-3. A) Bacterial richness (observed operational taxonomic units, OTUs). B) Chao and C) Shannon index of observed operational taxonomic units showed the *α*-diversity of the microbial community. D) PCoA indicates the similarity or difference in the species composition of the gut microbiota of UC mice in different treatment groups based on OTU levels. E) The Venn diagram of species among the three groups. F) Community histograms characterizing microbial composition at the phylum level. G) Heatmap exhibited the relative abundance of microbial compositional profiling at a family level. H) Relative abundance of microbiota with significant changes at the family level. I) Relative abundance of microbiota with significant changes at the genus level. n = 5 for each group. J) EMNs-gel-3 regulates the microenvironment of inflamed intestinal sites by mitigating inflammatory responses and alleviating intestinal flora imbalance.

phylum abundance. The relative abundance of *Firmicutes* increased significantly compared to the control group, consistent with trends reported in the literature for bacterial microbial therapy [46]. Next, specific bacteria were quantitatively analyzed at the family and genus levels (Fig. 7H and I). Treatment with EMNs-gel-3 significantly retained the relative abundance of *Muribaculaceae* (a major mucin monosaccharide forager that acts as an ecological gatekeeper in healthy guts) [47], and *Prevotellaceae* (a key contributor to short-chain fatty acid production, antioxidant, and anti-inflammatory processes) [48]. Additionally, *unclassified_Clostridia_UCG_014*, a group of opportunistic pathogens associated with gut dysbiosis and inflammation, showed a marked decrease compared to the control group [49]. At the genus level, the EMNs-gel-3 treatment group exhibited a significant increase in the relative abundance of beneficial bacteria such as *Lachnospiraceae_NK4A136_group* and *Alloprevotella* compared to the control group, while the relative abundance of potentially harmful bacteria like *Bacteroides* decreased, mirroring trends reported in the literature for patients with curative UC [50,51]. These results suggested that EMNs-gel-3 could optimize the composition of the gut microbiota in mice. The AP and phenolic hydroxyl groups present in EMNs-gel-3 play a crucial role in modulating the inflammatory process by regulating the overexpression of MMPs and reactive ROS at sites of inflammation [52]. By reducing oxidative stress and dampening inflammatory responses, EMNs-gel-3 aids in restoring immune homeostasis and thus promotes the healing of inflammation. Furthermore, EMNs-gel-3 positively affects the gut microbiota by increasing the relative abundance of beneficial bacteria and decreasing that of harmful bacteria (refer to Fig. 7J). These findings indicate that EMNs-gel-3 is an effective therapeutic agent for mitigating intestinal inflammation and enhancing the repair of injured intestinal tissue.

3. Conclusion

This study presented a sandcastle worms-inspired coacervate that could suppress ulcer bleeding and intestinal inflammation by generating hydrogel barriers on inflammatory sites, due to MMPs-triggered release of Fe^{3+} and subsequent generation of Fe^{3+} mediated rearrangement of the polymer network. The rheology analysis and adhesion mechanical evaluations showed that EMNs-gel-3 could form robust adhesion (peeling strength of 61.78 ± 4.27 Nm^{-1} and shear strengths of 57.81 ± 9.08 kPa) on the wet surface of the intestine within 300 s upon MMPs triggering. The in vitro dynamic modeling experiments demonstrated that EMNs-gel-3 could transform into hydrogel layers (81.83± 6.97 μm) at a locomotion speed of 50 mm/min which is much faster than the speed of food peristalsis in the normal intestine. Furthermore, the results of the ulcerative colitis mice model validated that EMNs-gel-3 could not only target the inflamed tissue to reduce delayed hemorrhage but also modulate intestinal inflammation by decreasing pro-inflammatory cytokines and accelerating M2 differentiation. Meanwhile, the in vitro and in vivo biocompatibility and metabolic assessments illustrated that the sandcastle worms-inspired coacervate displayed no obvious adverse effects. In addition, we envision that EMNs-gel can serve as a platform by incorporating a range of therapeutics for sustained drug delivery and detection of intestinal ulcers. Overall, this in-situ hydrogelation strategy inspired by sandcastle worms provides a versatile and potent approach for the future design of oral targeting coacervate.

Ethics approval and consent to participate

All animal experiments were performed in accordance with the protocols approved by the European Union Animal Experimentation Directive 2010/63/EU and by the protocols approved by the National Center for Experimental Teaching of Animal Science, Southwest University, China. The approval number is SWU_LAC_202110616. All mice and rats were purchased from Hunan Saijia Laboratory Animal Co. All animal experiments were approved by the Ethics Committee for Animal Experiments of Southwest University (Approval No. SYXK 2020-0006) and were conducted in accordance with the committee's guidelines for animal handling.

CRediT authorship contribution statement

Yuqi Peng: Writing – original draft, Methodology, Data curation, Conceptualization. **Xiaofen Luo:** Validation, Methodology. **Xinyu Wang:** Validation, Methodology. **Enling Hu:** Writing – review & editing. **Ruiqi Xie:** Writing – review & editing. **Fei Lu:** Data curation, Formal analysis. **Weiwei Ding:** Validation, Investigation. **Fangyin Dai:** Project administration, Funding acquisition. **Guangqian Lan:** Project administration, Funding acquisition. **Bitao Lu:** Writing – review & editing, Investigation, Conceptualization, Formal analysis.

Declaration of competing interest

The authors declare that they have no known competing financial interests or personal relationships that could have appeared to influence the work reported in this paper.

Acknowledgments

Funding: This study was supported by the Chongqing Postdoctoral International Exchange Training Program (7820100997), the Fundamental Research Funds for Central Universities (Nos. SWU-XDPY22010), the National College Students Innovation and Entrepreneurship Training Program (202310635114), the National Natural Science Foundation of China (No. 81703424), and the Chongqing Graduate Student Research Innovation Project (CYB21121).

Appendix A. Supplementary data

Supplementary data to this article can be found online at https://doi.org/10.1016/j.bioactmat.2024.08.020.

References

[1] G. Chen, F. Wang, M. Nie, H. Zhang, H. Zhang, Y. Zhao, Roe-inspired stem cell microcapsules for inflammatory bowel disease treatment, Proc. Natl. Acad. Sci. U. S. A. 118 (43) (2021).
[2] X. Yan, L. Meng, X. Zhang, Z. Deng, B. Gao, Y. Zhang, M. Yang, Y. Ma, Y. Zhang, K. Tu, M. Zhang, Q. Xu, Reactive oxygen species-responsive nanocarrier ameliorates murine colitis by intervening colonic innate and adaptive immune responses, Mol. Ther. 31 (5) (2023) 1383–1401.
[3] S. Liu, Y. Cao, L. Ma, J. Sun, L. Ramos-Mucci, Y. Ma, X. Yang, Z. Zhu, J. Zhang, B. Xiao, Oral antimicrobial peptide-EGCG nanomedicines for synergistic treatment of ulcerative colitis, J. Contr. Release 347 (2022) 544–560.
[4] O. Olen, R. Erichsen, M.C. Sachs, L. Pedersen, J. Halfvarson, J. Askling, A. Ekbom, H.T. Sorensen, J.F. Ludvigsson, Colorectal cancer in ulcerative colitis: a Scandinavian population-based cohort study, Lancet 395 (10218) (2020) 123–131.
[5] D. Zhong, D. Zhang, W. Chen, J. He, C. Ren, X. Zhang, N. Kong, W. Tao, M. Zhou, Orally deliverable strategy based on microalgal biomass for intestinal disease treatment, Sci. Adv. 7 (48) (2021) eabi9265.
[6] Y. Zhou, Z. Chen, D. Zhao, D. Li, C. He, X. Chen, A pH-triggered self-unpacking capsule containing zwitterionic hydrogel-coated MOF nanoparticles for efficient oral exendin-4 delivery, Adv. Mater. 33 (32) (2021) e2102044.
[7] X. Wang, M. Jiao, F. Tian, X. Lu, H. Xiong, F. Liu, Y. Wan, X. Zhang, H. Wan, A biomimetic nanoplatform with improved inflammatory targeting behavior for ROS scavenging-based treatment of ulcerative colitis, Adv. Healthcare Mater. 12 (29) (2023) e2301450.
[8] Y. Zhang, Y. Wu, Y. Yan, Y. Ma, L. Tu, J. Shao, X. Tang, L. Chen, G. Liang, L. Yin, Dual-targeted nanoparticle-in-microparticle system for ulcerative colitis therapy, Adv. Healthcare Mater. 12 (31) (2023) e2301518.
[9] R.P. Hirten, B.E. Sands, New therapeutics for ulcerative colitis, Annu. Rev. Med. 72 (2021) 199–213.
[10] H. He, Q. Qin, F. Xu, Y. Chen, S. Rao, C. Wang, X. Jiang, X. Lu, C. Xie, Oral polyphenol-armored nanomedicine for targeted modulation of gut microbiota-brain interactions in colitis, Sci. Adv. 9 (21) (2023) eadf3887.
[11] Q. Nie, C. Li, Y. Wang, Y. Hu, W. Pu, Q. Zhang, J. Cai, Y. Lin, G. Li, C. Wang, L. Li, Y. Dou, J. Zhang, Pathologically triggered in situ aggregation of nanoparticles for inflammation-targeting amplification and therapeutic potentiation, Acta Pharm. Sin. B 13 (1) (2023) 390–409.

[12] D. Bergemalm, E. Andersson, J. Hultdin, C. Eriksson, S.T. Rush, R. Kalla, A. T. Adams, A.V. Keita, M. D'Amato, F. Gomollon, J. Jahnsen, P. Ricanek, J. Satsangi, D. Repsilber, P. Karling, J. Halfvarson, Systemic inflammation in preclinical ulcerative colitis, Gastroenterology 161 (5) (2021) 1526–1539.
[13] K. Jakubowska, A. Pryczynicz, P. Iwanowicz, A. Niewinski, E. Maciorkowska, J. Hapanowicz, D. Jagodzinska, A. Kemona, K. Guzinska-Ustymowicz, Expressions of matrix metalloproteinases (MMP-2, MMP-7, and MMP-9) and their inhibitors (TIMP-1, TIMP-2) in inflammatory bowel diseases, Gastroenterol Res Pract 2016 (2016) 2456179.
[14] Y. Zhang, L. Wang, Z.D. Wang, Q. Zhou, X. Zhou, T. Zhou, Y.X. Guan, X. Liu, Surface-anchored microbial enzyme-responsive solid lipid nanoparticles enabling colonic budesonide release for ulcerative colitis treatment, J. Nanobiotechnol. 21 (1) (2023) 145.
[15] C. Zhang, Z. Chen, Y. He, J. Xian, R. Luo, C. Zheng, J. Zhang, Oral colon-targeting core-shell microparticles loading curcumin for enhanced ulcerative colitis alleviating efficacy, Chin. Med. 16 (1) (2021) 92.
[16] J. Li, T. Wang, A.R. Kirtane, Y. Shi, A. Jones, Z. Moussa, A. Lopes, J. Collins, S. M. Tamang, K. Hess, R. Shakur, P. Karandikar, J.S. Lee, H.W. Huang, A. Hayward, G. Traverso, Gastrointestinal synthetic epithelial linings, Sci. Transl. Med. 12 (558) (2020).
[17] P. Zhao, X. Xia, X. Xu, K. Leung, A. Rai, Y. Deng, B. Yang, H. Lai, X. Peng, P. Shi, H. Zhang, P. Chiu, L. Bian, Nanoparticle-assembled bioadhesive coacervate coating with prolonged gastrointestinal retention for inflammatory bowel disease therapy, Nat. Commun. 12 (1) (2021) 7162.
[18] X. Peng, Y. Li, T. Li, Y. Li, Y. Deng, X. Xie, Y. Wang, G. Li, L. Bian, Coacervate-derived hydrogel with effective water repulsion and robust underwater bioadhesion promotes wound healing, Adv. Sci. 9 (31) (2022) 2203890.
[19] J.N. Chu, G. Traverso, Foundations of gastrointestinal-based drug delivery and future developments, Nat. Rev. Gastroenterol. Hepatol. 19 (4) (2022) 219–238.
[20] Y. Lee, T.E. Deelman, K. Chen, D. Lin, A. Tavakkoli, J.M. Karp, Therapeutic luminal coating of the intestine, Nat. Mater. 17 (9) (2018) 834–842.
[21] R.J. Stewart, C.S. Wang, I.T. Song, J.P. Jones, The role of coacervation and phase transitions in the sandcastle worm adhesive system, Adv. Colloid Interface Sci. 239 (2017) 88–96.
[22] S. Chen, Q. Guo, J. Yu, Bio-inspired functional coacervates, Aggregate 3 (6) (2022) e293.
[23] S. Kaur, G.M. Weerasekare, R.J. Stewart, Multiphase adhesive coacervates inspired by the Sandcastle worm, ACS Appl. Mater. Interfaces 3 (4) (2011) 941–944.
[24] D. Zhang, J. Liu, Q. Chen, W. Jiang, Y. Wang, J. Xie, K. Ma, C. Shi, H. Zhang, M. Chen, J. Wan, P. Ma, J. Zou, W. Zhang, F. Zhou, R. Liu, A sandcastle worm-inspired strategy to functionalize wet hydrogels, Nat. Commun. 12 (1) (2021) 6331.
[25] W. Zhang, Y. Zhou, Y. Fan, R. Cao, Y. Xu, Z. Weng, J. Ye, C. He, Y. Zhu, X. Wang, Metal-organic-framework-based hydrogen-release platform for multieffective Helicobacter pylori targeting therapy and intestinal flora protective capabilities, Adv. Mater. 34 (2) (2022) e2105738.
[26] S. Zhang, J. Ermann, M.D. Succi, A. Zhou, M.J. Hamilton, B. Cao, J.R. Korzenik, J. N. Glickman, P.K. Vemula, L.H. Glimcher, G. Traverso, R. Langer, J.M. Karp, An inflammation-targeting hydrogel for local drug delivery in inflammatory bowel disease, Sci. Transl. Med. 7 (300) (2015) 300ra128.
[27] R. Ellerbrock, M. Stein, J. Schaller, Comparing amorphous silica, short-range-ordered silicates and silicic acid species by FTIR, Sci. Rep. 12 (1) (2022) 11708.
[28] E. Vassallo, A. Cremona, F. Ghezzi, F. Dellera, L. Laguardia, G. Ambrosone, U. Coscia, Structural and optical properties of amorphous hydrogenated silicon carbonitride films produced by PECVD, Appl. Surf. Sci. 252 (22) (2006) 7993–8000.
[29] Y. Yan, V. Sencadas, T. Jin, X. Huang, J. Chen, D. Wei, Z. Jiang, Tailoring the wettability and mechanical properties of electrospun poly(l-lactic acid)-poly (glycerol sebacate) core-shell membranes for biomedical applications, J. Colloid Interface Sci. 508 (2017) 87–94.
[30] S. Chen, S. Liu, L. Zhang, Q. Han, H. Liu, J. Shen, G. Li, L. Zhang, Y. Yang, Construction of injectable silk fibroin/polydopamine hydrogel for treatment of spinal cord injury, Chem. Eng. J. 399 (2020) 125795.
[31] L. Li, H. Wang, J. Ye, Y. Chen, R. Wang, D. Jin, Y. Liu, Mechanism Study on Nanoparticle Negative Surface Charge Modification by Ascorbyl Palmitate and its Improvement of Tumor Targeting Ability Molecules, 2022.
[32] D.G. Barrett, D.E. Fullenkamp, L. He, N. Holten-Andersen, K.Y. Lee, P. B. Messersmith, pH-based regulation of hydrogel mechanical properties through mussel-inspired chemistry and processing, Adv. Funct. Mater. 23 (9) (2013) 1111–1119.
[33] J. Yang, S.M. Cohen, M. Kamperman, Jack of all trades: versatile catechol crosslinking mechanisms, Chem. Soc. Rev. 43 (24) (2014) 8271–8298.
[34] T. Wong, S.H. Kang, S.K.Y. Tang, E.J. Smythe, B.D. Hatton, A. Grinthal, J. Aizenberg, Bioinspired self-repairing slippery surfaces with pressure-stable omniphobicity, Nature 477 (7365) (2011) 443–447.
[35] J. Sapudom, M. Kongsema, A. Methachittipan, S. Damrongsakkul, S. Kanokpanont, J.C.M. Teo, M. Khongkow, K. Tonsomboon, P. Thongnuek, Degradation products of crosslinked silk fibroin scaffolds modulate the immune response but not cell toxicity, J. Mater. Chem. B 11 (16) (2023) 3607–3616.
[36] J. Brown, C.L. Lu, J. Coburn, D.L. Kaplan, Impact of silk biomaterial structure on proteolysis, Acta Biomater. 11 (2015) 212–221.
[37] Z. Yin, H. Liu, M. Lin, W. Xie, X. Yang, Y. Cai, Controllable performance of a dopamine-modified silk fibroin-based bio-adhesive by doping metal ions, Biomed. Mater. 16 (4) (2021).
[38] L. Großmann, K. Springub, L. Krüger, F. Winter, A. Rump, M. Kromrey, R. Bülow, N. Hosten, J. Dressman, W. Weitschies, M. Grimm, Is there a fast track ("Darmstrasse") for fluids in the small intestine? Evidence from magnetic resonance imaging, Eur. J. Pharm. Biopharm. 198 (2024) 114277.
[39] A.M. Haase, T. Gregersen, L.A. Christensen, J. Agnholt, J.F. Dahlerup, V. Schlageter, K. Krogh, Regional gastrointestinal transit times in severe ulcerative colitis, Neuro Gastroenterol. Motil. 28 (2) (2016) 217–224.
[40] G. Hounnou, C. Destrieux, J. Desme, P. Bertrand, S. Velut, Anatomical study of the length of the human intestine, Surg. Radiol. Anat. 24 (5) (2002) 290–294.
[41] J. Worsoe, L. Fynne, T. Gregersen, V. Schlageter, L.A. Christensen, J.F. Dahlerup, N.J. Rijkhoff, S. Laurberg, K. Krogh, Gastric transit and small intestinal transit time and motility assessed by a magnet tracking system, BMC Gastroenterol. 11 (2011) 145.
[42] P. Fan, Q. Dong, J. Yang, Y. Chen, H. Yang, S. Gu, W. Xu, Y. Zhou, Flexible dual-functionalized hyaluronic acid hydrogel adhesives formed in situ for rapid hemostasis, Carbohydr. Polym. 313 (2023) 120854.
[43] Y. Li, L. Yang, Y. Hou, Z. Zhang, M. Chen, M. Wang, J. Liu, J. Wang, Z. Zhao, C. Xie, X. Lu, Polydopamine-mediated graphene oxide and nanohydroxyapatite-incorporated conductive scaffold with an immunomodulatory ability accelerates periodontal bone regeneration in diabetes, Bioact. Mater. 18 (2022) 213–227.
[44] L. Zhang, G. Li, B. Lin, H. He, R. Zhou, W. Jiang, Ascorbyl palmitate ameliorates inflammatory diseases by inhibition of NLRP3 inflammasome, Int. Immunopharm. 131 (2024) 111915.
[45] W. Zeng, D. He, Y. Xing, J. Liu, N. Su, C. Zhang, Y. Wang, X. Xing, Internal connections between dietary intake and gut microbiota homeostasis in disease progression of ulcerative colitis: a review, Food Sci. Hum. Wellness 10 (2) (2021) 119–130.
[46] M. Schirmer, A. Garner, H. Vlamakis, R.J. Xavier, Microbial genes and pathways in inflammatory bowel disease, Nat. Rev. Microbiol. 17 (8) (2019) 497–511.
[47] F.C. Pereira, K. Wasmund, I. Cobankovic, N. Jehmlich, C.W. Herbold, K.S. Lee, B. Sziranyi, C. Vesely, T. Decker, R. Stocker, B. Warth, M. von Bergen, M. Wagner, D. Berry, Rational design of a microbial consortium of mucosal sugar utilizers reduces Clostridiodes difficile colonization, Nat. Commun. 11 (1) (2020) 5104.
[48] W. Li, Y. Zhang, M. Chen, X. Guo, Z. Ding, The antioxidant strain Lactiplantibacillus plantarum AS21 and Clostridium butyricum ameliorate DSS-induced colitis in mice by remodeling the assembly of intestinal microbiota and improving gut functions, Food Funct. 15 (4) (2024) 2022–2037.
[49] J. Wang, Z. Jia, W. Pan, J. Hu, Crotonis Fructus-induced gut microbiota and serum metabolic disorders in rats, Appl. Microbiol. Biotechnol. 107 (22) (2023) 6949–6962.
[50] T. Konikoff, U. Gophna, Oscillospira: a central, enigmatic component of the human gut microbiota, Trends Microbiol. 24 (7) (2016) 523–524.
[51] C. Yan, S. Huang, H. Ding, E. Kwek, J. Liu, Z. Chen, K.Y. Ma, Z. Chen, Adverse effect of oxidized cholesterol exposure on colitis is mediated by modulation of gut microbiota, J. Hazard Mater. 459 (2023) 132057.
[52] B. Lubis, A. Lelo, P. Amelia, A. Prima, The effect of thiamine, ascorbic acid, and the combination of them on the levels of matrix metalloproteinase-9 (MMP-9) and tissue inhibitor of matrix metalloproteinase-1 (TIMP-1) in sepsis patients, Infect. Drug Resist. 15 (2022) 5741–5751.